補助人工心臓適応患者の生存率

東洋紡製左室脱血方式の左心補助人工心臓を心臓移植対象者に装着した症例においては、最長の補助期間は3年11ヶ月ですが、心臓移植あるいは補助人工心臓装着により自己心臓機能が改善し離脱することで、長期生存が得られており、国立循環器病センターでの5年生存率は38.9%となっています。また、米国では心臓移植適応とならない末期心不全患者さんを対象に、体内植込み型左心補助人工心臓（LVAS）のハートメートVEと、最大の内科的治療の成績を比較する二重盲検試験が行われ、LVAS装着患者さんの成績が良好でした。この結果より、2003年秋には、ハートメートVEが心臓移植の適応とならない末期心不全患者さんに対するポンプ装着下日常生活への復帰をめざす機器として認められました。わが国においても、長期在宅治療を目指したLVASの適応について検討が進められています。

■心臓移植の対象となる患者
東洋紡製左室脱血方式の
左心補助人工心臓症例

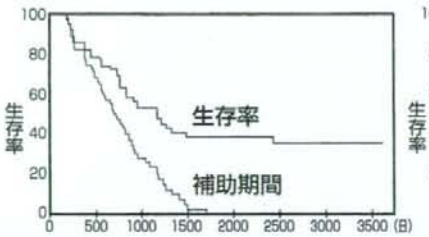

（国立循環器病センター）

■心臓移植の対象とならない患者
体内植込み型左心補助人工心臓（ハートメートVE）症例と
内科的治療症例の比較

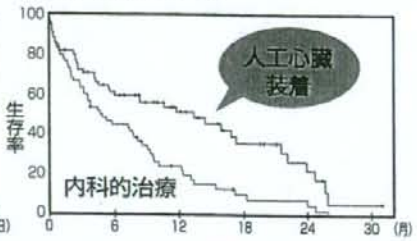

出典：N Engl J Med 2001;345:1435-43

長期使用目的で用いられる補助人工心臓

ノバコアLVASは2004年から心臓移植施設における移植登録待機例での適応に対し、健康保険が適用されるようになりました。しかし、治験から8年を経過し、用いるバッテリーが旧式となったため提供が受けられなくなり、新たな適応ができなくなりました。新しい人工心臓としてわが国では2種の遠心ポンプを用いた無拍動流体内設置携帯型LVASの開発が進められており、エヴァハートはわが国で治験が開始され、デュラハートは欧州での治験が終わり、現在わが国での治験準備中です。また、米国で開発された軸流血液ポンプジャービック2000がわが国に導入されており、現在治験準備が進められています。

拍動流体外設置型LVAS
〈東洋紡製国循型〉

拍動流体内設置携帯型LVAS

無拍動流体内設置携帯型LVAS
新しい人工臓器

人工心臓

人工心臓の開発は続けられ、より性能の高いものを目指している

心臓の機能が著しく低下し、内科的あるいは外科的治療に反応しない重症の心不全になると、心臓機能の機械的な補助や置換が必要となります。このため、人工心臓や心臓移植の研究から臨床応用が進められてきました。

人工心臓には、自然心臓を摘出してとりかえる「全置換型人工心臓」と、自然心臓を残してその近くに設置して機能の100%までの代行を行う「補助人工心臓」があります。両者の開発、臨床応用が行われていますが、現状では植込み携帯型の「補助人工心臓」の開発・臨床応用が主に行なわれています。また、これまでは自然心臓と同じように拍動をもったシステムが主体でしたが、小型化や長期安定した機能が期待できる「無拍動流ポンプ」を用いた血液ポンプの開発・臨床応用が積極的に進められています。

わが国の現状

わが国では、1980年に東京大学型補助人工心臓が、また1982年に国立循環器病センター型補助人工心臓が臨床応用されました。その後、それぞれ日本ゼオン・アイシン精機製(東京大学型)、東洋紡製(国立循環器病センター型)として1986年に治験が開始されました。両者とも世界に先駆けて1990年に製造承認を得、1994年には急性心不全に対する適応に対し、健康保険が適用されるようになりました。また、1992年からは心臓移植の対象となる心筋症に対しても適応されるようになり、現在では半数程度が心筋症への適応となり、東洋紡型が最も多く用いられています。

年次別補助人工心臓適用症例数の推移

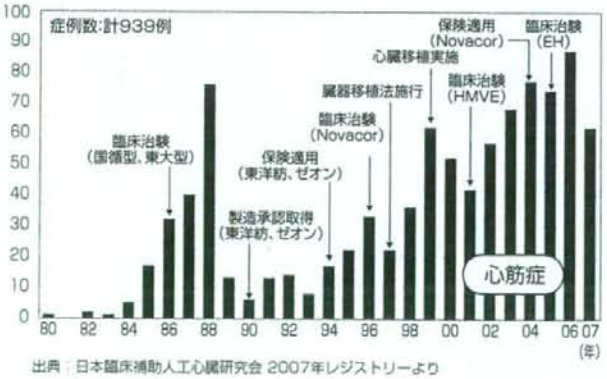

出典：日本臨床補助人工心臓研究会 2007年レジストリーより

血液ポンプ別症例数

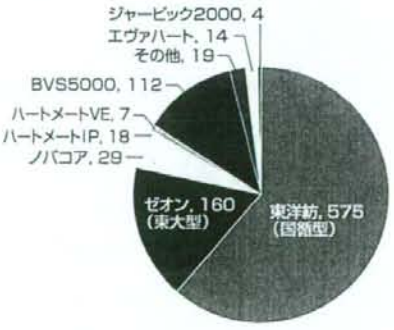

出典：日本臨床補助人工心臓研究会 2007年レジストリーより

移植後の活動制限

米国における心臓移植後の身体活動に関する移植後7年までの調査において、90%前後の人々が活動制限なしの生活を送っています。

出典： J Heart Lung Transplant 2007;26: 769-781

世界および日本における心臓移植の累積生存率

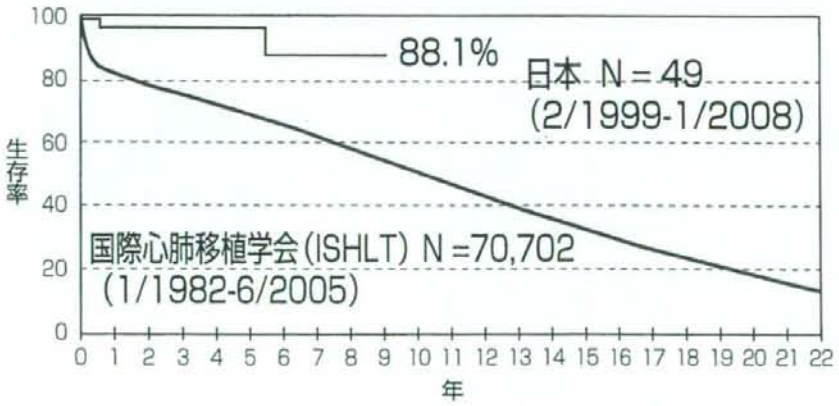

出典：ISHLTのデータ／J Heart Lung Transplant 2007;26: 769-781
日本心臓移植研究会報告 移植 2007;42: 427-429より改変

心臓移植医療

49例の心臓移植が7施設で行われている

心臓の機能が著しく低下し、内科的あるいは外科的治療に反応しない重症の心不全になると、心臓機能の機械的な補助や置換が必要となります。このため、人工心臓や心臓移植の研究から臨床応用が進められてきました。心臓移植では脳死体からの臓器提供がなされるときに、受け手側との血液型や体格などが適合した場合に行われます。1967年に第1例目が南アフリカで行われ、以後種々の検討が行われ、1980年代からは欧米において重症心不全に対する治療選択のひとつとして受け入れられ、年間4000例以上行われるようになりました。現在では提供数に応じて3000例程度施行されています。わが国では1997年に臓器移植法が制定され、1999年に第1例目が施行されてからこれまでに49例の心臓移植が7施設で行われており、施行数は少ないもののその成績は国際レジストリーよりも良好となっています。心臓移植は、一生涯免疫抑制剤を服用する必要があり、定期的な検査が必要ですが、適合者があれば新生児から成人まで行うことができます。

わが国における心臓移植手術

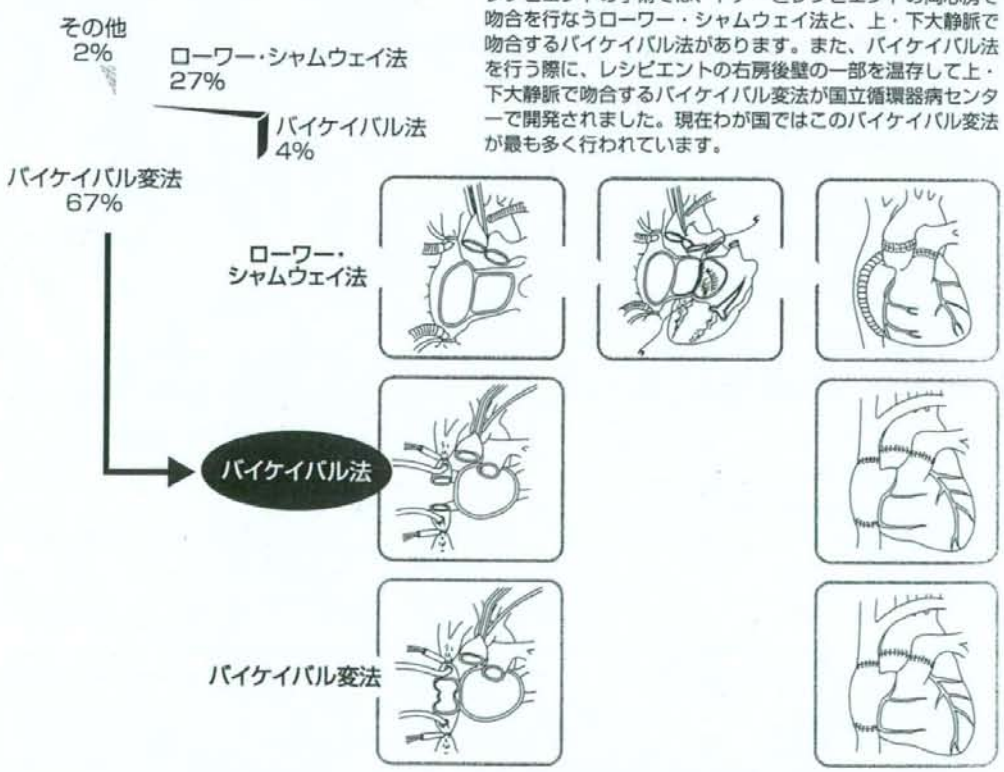

レシピエントの手術では、ドナーとレシピエントの両心房で吻合を行なうローワー・シャムウェイ法と、上・下大静脈で吻合するバイケイバル法があります。また、バイケイバル法を行う際に、レシピエントの右房後壁の一部を温存して上・下大静脈で吻合するバイケイバル変法が国立循環器病センターで開発されました。現在わが国ではこのバイケイバル変法が最も多く行われています。

出典：日本心臓移植研究会報告 移植 2007;42: 427-429より改変

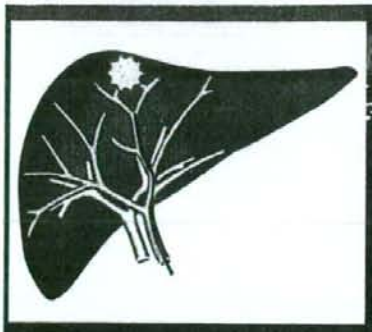

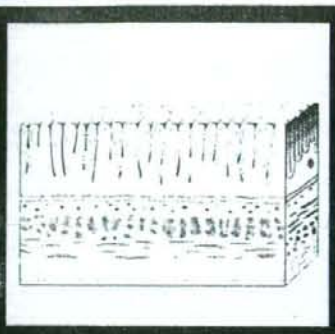

ビジュアル版

3大疾病の教科書

がん・心臓病・脳卒中をストップ！

三省堂

39) D. A. Hammer *et al.*, *Biophys. J.*, **63**, 35 (1992)
40) C. C. Roberts *et al.*, *Biophys. J.*, **58**, 841 (1990)

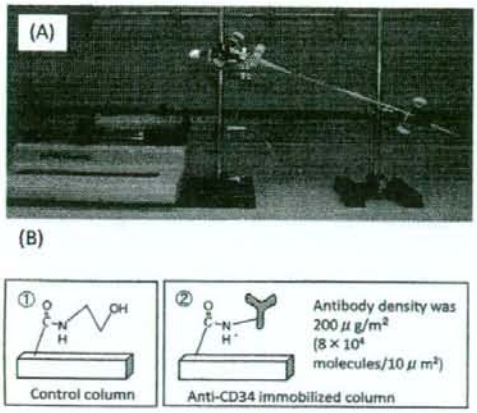

図2　(A) 細胞分離カラムシステムの外観
(B) 分離カラムの構造（①コントロールカラム、②抗体固定化カラム）

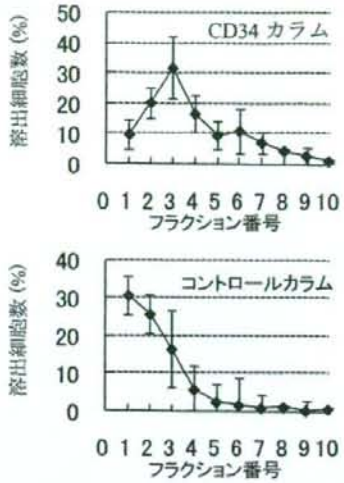

図3　マウス由来MSCを抗CD34抗体修飾細胞分離カラムにより溶出させた時のプロファイル

5.5　おわりに

細胞懸濁液から幹細胞を分離する場合，大きく分けて2つのアプローチが存在しているものと考えている。1つは高純度で均一なMSCを分離する手法，2つ目としてはMSC成分を含む細胞ポピュレーションを分離する手法である。MSCの機能やその性質を本質的に理解するためには，高純度で得られたMSCを用いて分化能や表面マーカーの発現量を詳細に検討する必要がある。一方で，MSCによる治療効果を検討する場合，大量のMSCが必要となるので，簡便な操作により大量に細胞を分離できることが望まれる。今後，治療メカニズムの検証や安全で効率的な移植治療法の実現化を目指すためにも組織再生を担う幹細胞を高純度で分離できるデバイスの開発や新たな分離メカニズムの開発はますます重要になるものと思われる。

文　　献

1) J. A. Thomson *et al.*, *Science*, **282**, 1145 (1998)
2) M. F. Pittenger *et al.*, *Science*, **284**, 143 (1999)
3) Y. Jiang *et al.*, *Nature*, **418**, 41 (2002)
4) K. Takahashi, *Cell*, **131**, 861 (2007)

ーションを分離するものである。同様のメカニズムとして，Changらの報告でもマイクロ流路内に配置した柱にリガンドを固定化し，細胞を流すことでリガンドと結合した細胞を分離できることが報告されている[27]。このような手法は，特定の細胞を基材上に補足することで分離を達成するため，Digital型分離法として分類することができる。

これに対して筆者らのグループでは，固定化リガンドと細胞表面マーカーとの連続的な相互作用を利用して細胞ポピュレーションを分離する手法を開発している。これは，Hydrodynamicsにより細胞をリガンド固定化界面へ流すことでリガンドと特異的に結合した細胞がshear stressを受け回転運動（ローリング）し，細胞表面レセプター量に応じた細胞分離が達成されるものである。このローリング速度は表面レセプター量に応じて変化するため，Continuous型の細胞分離として分類することができる。詳細は後述する。

他にも，FACSを利用してHoechst 33342の染色挙動から分離されるSP （side population）細胞を採取して幹細胞を分離する方法がある。細胞の表面マーカーが同定されているHSC, EPCの場合では，比較的容易に均一な細胞ポピュレーションを分離することが可能となる。しかしMSCの場合では，未分化度が高くさまざまな表面マーカーの発現が報告されているにも関わらずコンセンサスな結果が得られていない。成熟した細胞の場合では特定の表面マーカーの発現の有無により細胞ポピュレーションが規定されるが，未分化な細胞の場合，表面マーカーの発現量は連続的に変化するものと思われる。MSCやHSCにおいてCD34の発現は，*in vitro*の培養期間や個体の年齢によって一定に発現しないことを示すデータも報告されている[28, 29]。このような観点から筆者らのグループでは，細胞表面マーカーの発現量に応じて連続的に細胞ポピュレーションを分離可能な細胞分離カラムシステムの開発を進めている。

5.4　細胞分離カラムの開発

これまでに筆者らのグループでは，表面マーカー発現量に応じて細胞を分離する細胞分離システムを開発している。これは表面マーカーに対する抗体を平面基板上へ固定化し，検体となる細胞をローリングさせることで，細胞表面マーカーと固定化抗体との相互作用を誘起し目的細胞ポピュレーションを分離する。この相互作用は，血管内で炎症部位付近に白血球が集積する場合に観察される白血球ローリング現象として知られており[30]，セレクチンとの相互作用により白血球のローリング速度は著しく減少する[31, 32]。この原理を応用してGreenbergらは，表面マーカーの有無によるローリング速度の差を利用して細胞分離する手法を報告している[33]。また，Langerらは平面基板上へリガンドを2次元に固定化し，作製したパターン化リガンド上で細胞ローリングさせることにより目的の細胞ポピュレーションを分離するマイクロチップを開発して

ヘテロな細胞の中から目的の機能を有する細胞ポピュレーションを分けるための「細胞分離」である。組織幹細胞は細胞外マトリックスや他の成熟細胞とともに存在しているため，細胞成分を組織より採取し，その後幹細胞ポピュレーションを分離する必要がある。固形の臓器や組織から細胞を採取する場合，酵素や機械的切断により細胞懸濁液を調製する必要があるが，血液や骨髄などの液体組織では，吸引により比較的簡単に細胞懸濁液を調製できる。MSCは骨髄だけでなく脂肪組織にも存在することが報告されているが，患者から簡便に採取が可能な骨髄由来のMSCは細胞移植における有力な細胞ソースであろう。

最も重要なステップは，細胞懸濁液から移植に必要な細胞ポピュレーションのみを分離することであり，さまざまな手法が開発されている。目的の細胞ポピュレーションを分離するための細胞分離法を表2にまとめた。分離する場合の指標としては，細胞の物理的性質に基づくものと，生物学的性質に基づくものに分類されている[16]。また，細胞を分離する形式としてDigital型とContinuous型に分類した。Digital型とは，特定の指標に着目してヘテロな細胞懸濁液から1つの細胞ポピュレーションを分離する手法である。密度勾配遠心により採取される単核球細胞や，細胞表面マーカーの有無で磁気ビーズ法により分離される細胞ポピュレーションも，Digital型分離法として分類できる。これに対してContinuous型分離法とは，特定の指標に着目してその連続的な物理量により複数の細胞ポピュレーションを分離する手法である。この手法の研究例は少ないものの，連続磁場中において磁気ビーズで標識された細胞を標識量の違いに基づいて分離するデバイスや，細胞の電気的性質の違いにより細胞を分離する方法も報告されている。

表2　細胞分離技術

指　標	Force field	Type	名　称	内　容
物理的性質（細胞の大きさ，比重など）	Centrifngal	Digital	密度勾配遠心分離	単核球成分の分離
	Adhesion	Digital	Adhesion population	接着細胞分画の分離
	Electronic	Continuous	DEP (Dielectrophoresis)	電場の中で誘電率の違いによる分離
		Digital	FACS (Fluorescence activated cell sorting)	表面抗原を蛍光ビーズで標識して分離
生物学的性質（表面マーカー）	Magnetic	Continuous	DMFF (Dipole Magnet Flow Fraction)	磁場の中で標識に基づく細胞分離
		Digital	MACS (Magnetic activated cell sorting)	表面抗原を磁気ビーズで標識して分離
	Hydrodynamic	Continuous	Column system	リガンド固定化界面で細胞ローリングにより特定のマーカー密度をもつ細胞を分離
		Digital	Membrane	分離膜で特定の細胞を分離

表1　幹細胞ソースとしての特徴

分化度	細胞	利点	欠点
未分化	胚性幹細胞	多分化能	テラトーマ形成 倫理的な問題
細胞の分化度	人工多能性幹細胞	倫理的問題の回避	テラトーマ形成
	間葉系幹細胞	組織より採取可能 自家移植が可能	単離・同定が困難
	造血幹細胞		分化できる組織が限定
成　熟			

5. 2. 1　胚性幹細胞（ES細胞）

1998年，Thomsonらのグループはヒト ES 細胞の樹立を報告した[1]。胚盤胞に形成される細胞塊から作製される ES 細胞は，神経系細胞[5]，血球系細胞[6]，心筋細胞[7, 8] などさまざまな組織細胞へと分化が可能である。しかし，ES 細胞の移植を考えた場合，分化能力が高い反面，目的以外の組織細胞へ分化する可能性も含まれており，奇形腫（テラトーマ）形成の危険性が危惧されている。このことから，ES 細胞を試験管内で目的組織へと分化させてから移植する必要がある。また，ES 細胞は受精卵より形成される胚盤胞から調製されるため，免疫拒絶や倫理的な問題も指摘されている。

5. 2. 2　人工多能性幹細胞（iPS細胞）

Yamanakaらのグループによって，ヒト繊維芽細胞に対して4つの遺伝子（Oct3/4，Sox2，Klf4，c-Myc）を発現させることで ES 細胞様の未分化な幹細胞へとリプログラミングできることが報告された[4]。作製された細胞は iPS 細胞として報告され，遺伝子の発現パターンや成熟細胞への分化，テラトーマ形成といった ES 細胞特有の性質を iPS 細胞も有していることが示されている。その後，ガン関連遺伝子である Myc の発現を必要としなくても iPS 細胞を作製できることが同グループより報告されている[9]。細胞移植ではテラトーマ形成が問題となるものの，患者自身の繊維芽細胞から幹細胞が作製可能であることから，倫理的な問題をクリアーできる技術として期待されている。

5. 2. 3　間葉系幹細胞（MSC）

Pittengerらのグループにより1999年に報告された MSC に関する研究[2] では，骨髄中に含ま

5　幹細胞分離法とポピュレーション解析

馬原　淳[*1]，山岡哲二[*2]

5.1　はじめに

次世代医療として着目されている再生医療は，生体の細胞や組織が有している再生能力を人為的に利用して，失われた機能や構造の再生を促す治療法である。細胞ソースとしては，患者自身から採取した間葉系幹細胞などの自己幹細胞が広く検討され，その臨床利用も始まっている。このような再生医療がさらに一般的な治療法となるためには，安全性が担保された均一な幹細胞ポピュレーションの調製が必須であり，組織の中でさまざまな細胞と混在している幹細胞を，未分化状態を維持したまま効率的に分離することが求められる。さらに，これらの体性幹細胞，あるいは，近年注目されているES細胞やiPS細胞を体外で目的の細胞に分化させて利用する場合には，分化誘導の過程でさまざまな分化ステージの細胞が出現するために，ここでも，均一な細胞ポピュレーションのみを抽出する必要がある。つまり幹細胞の単離・分離法は，再生医療の治癒効果の向上や安全性を担保するためにも極めて重要な操作となる。本項では再生医療で利用が期待されている幹細胞の分離法に焦点を絞り，その現状と最新の研究成果について紹介する。

5.2　再生医療における幹細胞

幹細胞研究の急速な発展は，再生医療や細胞移植治療の可能性を大きく広げた。1998年Thomsonらにより報告されたヒトES細胞樹立[1]，1999年のPittengerらによる間葉系幹細胞の分離と分化能についての報告[2]，2002年のVerfaillieらによる間葉系幹細胞の可塑性についての発見[3]，2007年Yamanakaらによる人工多能性幹細胞（iPS）の作製の成功[4]は，再生医療における細胞ソースの可能性として大きなインパクトを与えた。しかし，分子生物学分野における幹細胞の発見や分化に関する研究成果は，直ちに再生医療へと応用できるものではない。組織から採取した幹細胞を移植細胞ソースとして利用する場合，副作用がなく安定な治療効果を達成するためには，その純度，分化の均一性，感染の可能性を十分に考慮する必要がある。表1には種々の幹細胞の特徴を示した。未分化な細胞であれば種々の疾患に対して応用することができ，その中でも，自家細胞移植は最も安全性が担保しやすいものと考えられている。

＊1　Atsushi Mahara　国立循環器病センター研究所　先進医工学センター　生体工学部室員

＊2　Tetsuji Yamaoka　国立循環器病センター研究所　先進医工学センター　生体工学部部長

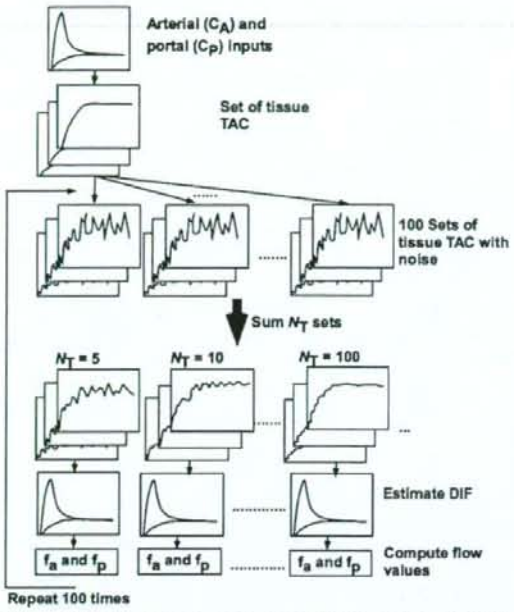

Fig. 3 Schematic diagram of the procedure to analyze statistical accuracy of hepatic arterial (f_a) and portal flow (f_p) values against noise on tissue curves. First, tissue time–activity curves (*TAC*) with noise were generated by imposing Gaussian noise on the set of ten hepatic tissue TACs. This procedure was repeated 100 times, and 100 sets of noisy tissue TACs were obtained. Next, the N_T (=5, 10, 20, 50, 100, and 200) sets of tissue TACs with the same flow value were summed. For each N_T, dual input function (*DIF*) was estimated. Then, arterial (f_a) and portal blood flow (f_b) values were computed using estimated DIF and tissue TACs. This procedure was repeated 100 times

each level of noise, DIF was estimated, as described. Then, arterial and portal vein blood flow values were computed as above, using estimated DIF and tissue TACs with f_a of 15 ml/100 g/min. This procedure was repeated 100 times, and the bias and deviation in values of arterial and portal vein flow results were calculated. Their bias and deviation was presented as a function of N_{tis}.

Experimental study

PET experiment

Fourteen pigs under anesthesia with weight 30.0±1.1 kg were studied. Data on glucose metabolism in these animals have been previously reported [13, 14]. Animals were deprived of food on the day prior to the study at 5:00 pm. Anesthesia was induced with ketamine (1.0 g) into neck muscles and maintained by ketamine and pancuronium (total of 1.5 g and 40 mg, respectively) administered intravenously during the experiment. Animals were intubated through a tracheostomy, and their respiration was controlled by a ventilator providing oxygen and normal room air (regulated ventilation, 16 breaths per minute). Catheters were inserted into the carotid artery for arterial blood sampling and the femoral vein for administration of $H_2{}^{15}O$. Splanchnic vessels were accessed by sub-costal incision; after dissection of the hepato-gastric ligament, purse string sutures were allocated to allow catheter insertion via a small incision in the portal vein. A catheter was inserted directly in the portal vein for portal vein blood sampling. Ultrasound-based flow-probes (Medi-Stim Butterfly Flowmeter, Medi-Stim AS) were placed around the portal vein and hepatic artery to determine blood velocity in each vessel. The diameter of the hepatic artery and portal vein were measured off-line from B-mode ultrasound images acquired using an Acuson Sequoia 512 mainframe with a 13-MHz B-mode linear array transducer. The area of the vessel was calculated assuming circular shape. Then, blood flow was obtained for each vessel during the PET scans. The surgical access was closed, and the distal catheter extremities were secured to the abdominal surface to avoid tip displacement. The animals were then transported to the PET center for tracer administration, liver imaging, and blood sampling. Vital signs, blood pressure, and heart rate were monitored throughout the study.

PET acquisition was carried out in 2D mode using an ECAT 931-08/12 scanner (CTI Inc, Knoxville, TN, USA) with a 10.5-cm axial field of view and a resolution of 6.7 mm (axial)×6.5 mm (in-plane) full width at half maximum. After transmission scan for attenuation correction, the dynamic scan was started after the injection of $H_2{}^{15}O$ (274 MBq, 30-s bolus injection), consisting of 20 frames with gradually increasing individual durations (6×5, 6×15, and 8×30 s).

During PET scanning, blood was withdrawn continuously from the carotid artery and portal vein through catheters (1.4 mm in inner diameter; length of tube was 900 mm to the detector and 60 mm in the detector sensitive region) by using a peristaltic pump (Scanditronix, Uppsala, Sweden) with a withdraw speed of 6 ml/min. Radioactivity concentrations in blood were measured with a BGO coincidence monitor system. The detectors had been cross-calibrated to the PET scanner via ion chamber [26].

At the end of the experimental period, animals were sacrificed by potassium chloride injection and anesthetic overdose, the abdominal cavity was rapidly accessed, and the whole liver was explanted and weighed and its volume was measured by water displacement; liver density was calculated as the ratio of organ weight-to-volume to derive the ultrasound-based flow to PET-equivalent unit (i.e., flow per unit of tissue volume).

The protocol was reviewed and approved by the Ethical Committee for Animal Experiments of the University of Turku.

Data processing

Dynamic sinogram data were corrected for dead time in each frame in addition to detector normalization. Tomographic images were reconstructed from corrected sinogram data by the median root prior reconstruction algorithm with 150 iterations and Bayesian coefficient of 0.3 [1]. Attenuation correction was applied with transmission data. A reconstructed image had 128×128×15 matrix size with a pixel size of 2.4 mm×2.4 mm and 6.7 mm with 20 frames.

Measured arterial and portal vein blood TACs were corrected for physical decay and dispersion [11] as τ=2.5 s, which was experimentally obtained and usually applied in our center. The arterial TAC corrected for decay and dispersion was then corrected for delay by fitting to a whole-liver tissue TAC [12]. The arterial curve obtained, $C_a(t)$, was used as the measured arterial input function. Then, the portal vein curve, corrected for dispersion (τ= 2.5 s) and delay with the same delay time for arterial TAC, $C_P(t)$, was fitted according to the following equation:

$$C_P(t) = k_g C_a(t + \Delta t_p) \otimes e^{-k_g (t+\Delta t_p)} \quad (8)$$

to obtain k_g and to account for the appearance time (Δt_p seconds) via the gut system. Obtained measured curves were directly fitted with Eqs. 1 and 2 to examine adequacy for a usage of model functions.

A region of interest (ROI) was placed on the whole region of the liver in a summed image and subsequently divided plane-by-plane into sub-regions of 700 pixels each, corresponding to 11–22 sub-regions. Sub-regions were created by extracting pixels firstly from horizontal then vertical directions inside the whole ROI in each slice. Each sub-region consisted of a single area with the same number of pixels. Tissue TACs in the sub-regions were extracted from dynamic images. Then, DIF was estimated according to the procedure introduced above. In the first step, initial values and boundary conditions for the non-linear fitting (PAW environment) for each parameter were 20,000 between 0.0000002 and 200,000,000 Bq/ml for A, 5 between 2 and 20 ml/min for $K_e(1+\alpha)$, 1 between −10 and 100 s for t_1, 20 between 1 to 60 s for t_2-t_1, 20 between 1 and 100 ml/min/g for f_a, 100 between 1 and 400 ml/min/g for f_b, and 0.05 between 0 and 1 ml/ml for V_0. In the second step, S^2 value in Eq. 6 was minimized, and the image-based input function was obtained. Areas under the curves (AUC) for measured and image-based inputs were calculated for 0 to 180 s. Their percent difference was calculated.

Perfusion values f_a and f_p were calculated by non-linear Gauss–Newton fitting method (PyBLD environment). Results obtained with the new technique were compared with (a) those obtained with the measured input function and (b) the ones from our independent reference method, i.e., ultrasonography, after their normalization to the organ volume to derive PET-equivalent units.

Statistical analysis

Data are shown individually or as mean±SD. The Student's paired t test was used for intra-individual comparisons of flow values. Regression analyses were performed according to standard techniques. A $p<0.05$ was considered to be significant. Differences between the flow values were calculated as $(f_X-f_Y)/f_X$ where f_X and f_Y are flow values from the non-invasive method and from the measured input or ultrasonography, respectively, and plotted in Bland–Altman plot [3].

Results

Simulation study

The biases in values of arterial, portal vein, and total blood perfusion due to a fixed k_g and delay time are presented in Fig. 4a and b as a function of the value of k_g and delay time, respectively. The error in total flow results did not exceed 10% for a ≤20% (i.e., 0.4–0.6 min^{-1}) difference between the fixed and the assumed (true) k_g and for a <10-s time delay.

The influence of noise and number of tissue TACs, i.e., the bias and deviation on both arterial and portal blood flow values, showed to be minimal for a number of tissue TACs of 10 to 20 at both noise levels (Fig. 5). As shown in Fig. 5, if the number of tissue TACs is increased, noise on each curve for input estimation becomes larger. On the other hand, a smaller number of tissue TAC corresponds to less information from tissue TAC in terms of variation of flow values. This result suggested that the optimal number of tissue TACs to be applied to preserve accuracy is in the above range, which is independent of the two noise levels. Among the five parameter composing the model input functions, the three parameters t_1, t_2, and r_a were determined with same accuracy, i.e., both the difference and deviation in those values were less than 1 s for t_1 and t_2 and 5% for r_a, respectively, for the noise level of 10%, independent of the number of tissue TACs. Bias and deviation of the remaining two parameters A and $K_e(1+\alpha)$ depended on the number of tissue TACs following the same tendency as the bias and deviation on blood flow values, as described above.

Experimental study

Reconstructed images are shown in Fig. 6, together with divided sub-regions. In the first step of our procedure, the

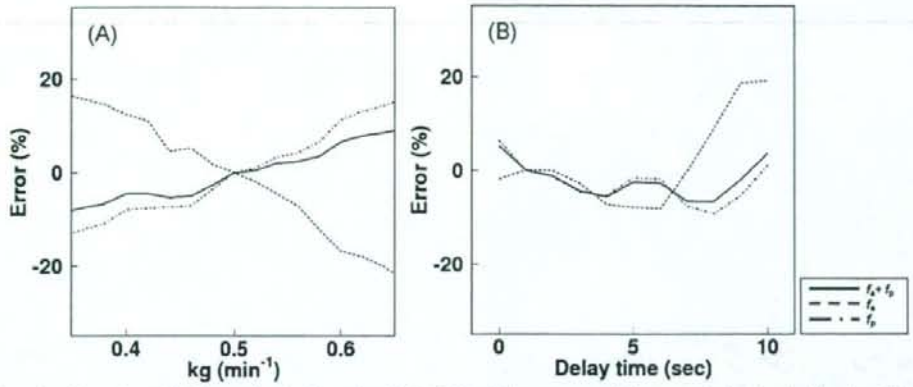

Fig. 4 Error in values of arterial (f_a), portal vein (f_p), and total (f_a+f_p) blood flow propagated from error in k_g (**a**) and delay time (**b**)

obtained value of t_1 from TACs extracted from sub-regions overlapping the vena cava (e.g., lower sub-region at upper left side image in Fig. 6) was 10 to 13 s earlier than the mean, and these TACs were omitted from further processing. The estimated t_2-t_1 was 27±3 s, which was similar to the tracer administration duration.

Figure 7 shows the curves of the model arterial and portal input functions (Eqs. 1 and 2) directly fitted to measured curves. The model functions for those were superimposable to measured curves, although both modeled curves slightly overestimated at the late times. This result suggested that the model function was almost adequate to use for the estimation of input.

The mean±SD of k_g was 0.497±0.153 ml/min/g and that of Δt_p was 0.7±5.1 s obtained by fitting the portal TAC using arterial TAC by Eq. 8.

Estimated, image-derived arterial and hepatic input functions were almost superimposable to the measured curves (Fig. 8). The mean±SD and range of difference of AUCs were −3.15±8.73% ranging from −13.5% to 17.9% and 1.47±8.87% ranging from −13.5% to 10.2% for arterial and portal input functions, respectively. The coefficient of variation of the estimated flow ratio between artery and portal vein in the first step across sub-regions was 26±9%. The mean±SD of that ratio across subjects was 0.15±0.07 and those from ultrasonography was 0.16±0.06, and paired t test showed no significant difference between them. This suggests supporting the assumption that the ratio between arterial and portal input defined in Eq. 5 relates to the flow values.

The Bland–Altman plot between values of hepatic arterial, portal, and total perfusion, as estimated by using the image-derived versus the measured blood curves, is shown in Fig. 9. This plot demonstrates a small overestimation by image-derived method with a bias of 0.01 and 0.07 ml/min/g for arterial and portal flow, respectively, and that 0.08 ml/min/g for total flow. Respective regression lines were the following: $y=0.00+1.09\ x$ ($r=0.97$, $p<$

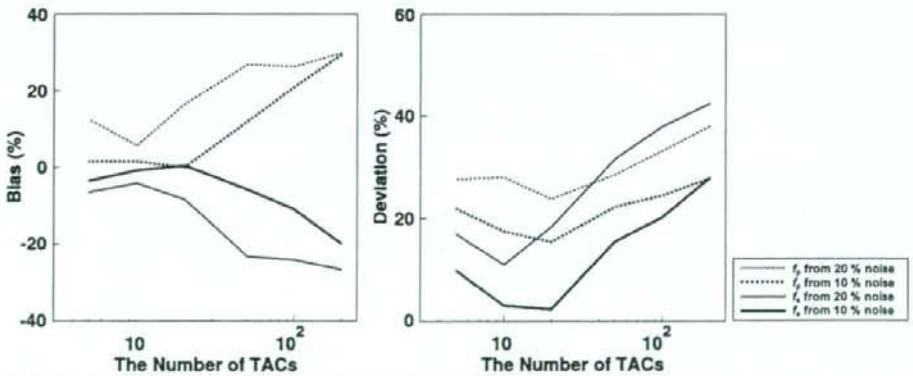

Fig. 5 Bias (*left*) and deviation (*right*) in the arterial and portal vein blood flow values as a function of the number of time–activity curves applied to the estimation of the input function

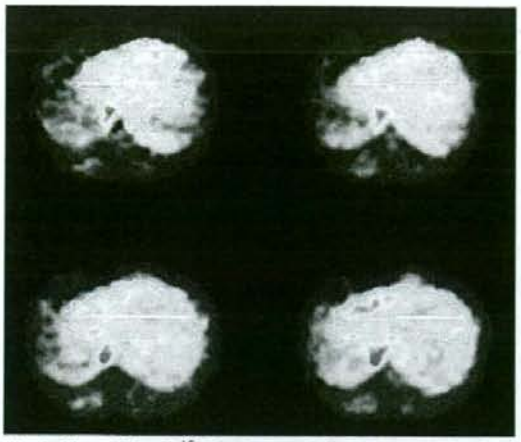

Fig. 6 View of liver $H_2{}^{15}O$ PET images in four slices and sub-regions (*solid line*). The small area with high activity levels on the mid-right and mid-left side of the image corresponds to the vena cava and aorta, respectively

0.001), $y=0.05+1.02\ x$ ($r=0.87$, $p<0.001$), and $y=0.02+1.06\ x$ ($r=0.90$, $p<0.001$). Paired t test showed no significant difference between the methods. Differences were $-6.8\pm20.0\%$, $-4.9\pm14.3\%$, and $-5.8\pm15.6\%$ for arterial, portal, and total blood flow values, respectively.

The Bland–Altman plot between values of hepatic arterial, portal, and total perfusion, as estimated by using the current method versus ultrasonography, is given in Fig. 10. This plot demonstrates an overestimation by image-derived method with a bias of 0.02 and 0.22 ml/min/g for arterial and portal flow, respectively, and that 0.24 ml/min/g for total flow. Respective regression lines were the following: $y=0.06+0.69\ x$ ($r=0.69$, $p=0.12$), $y=0.41+0.98\ x$ ($r=0.54$, $p=0.025$), and $y=0.24+0.97\ x$ ($r=$

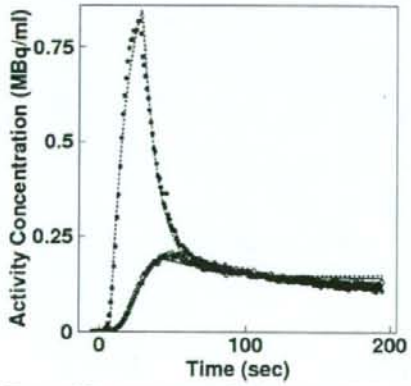

Fig. 7 Time–activity curves representing the arterial (*broken line*) and portal (*solid line*) model input functions (Eqs. 1 and 2) in comparison with the measured arterial (*black circles*) and portal (*open circles*) input functions

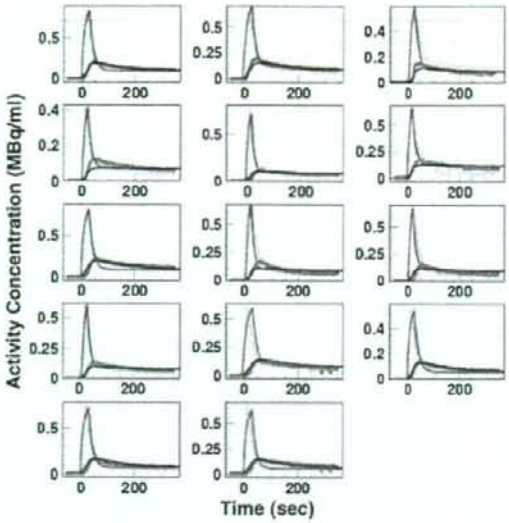

Fig. 8 Estimated arterial (*red line*) and portal vein (*blue line*) input functions from PET images and their comparison with measured arterial (plot in *light blue*) and portal input (plot in *pink*) functions

0.60, $p=0.022$). Again, paired t test showed no significant difference between the methods. Differences were $3.6\pm52.0\%$, $15.5\pm31.3\%$, and $16.9\pm33.0\%$ for values of arterial, portal, and total blood flow, respectively.

The total flow values ranged from 0.5 to 2 ml/min/g in the animals (Figs. 9 and 10). However, only two out of 14 showed smaller values of 0.5 ml/min/g (i.e., approximately 500 ml in the whole organ), which is still physiologically reasonable, while the great majority clustered between 1 and 2 ml/min/g.

Discussion

In the current work, we developed and validated a method to estimate the two components of the hepatic dual input function from liver $H_2{}^{15}O$ PET images and quantify hepatic perfusion. Computer simulations were used to evaluate the influence of assumptions, noise in raw data, and number and size of the regions of interest to be used in the analysis. After demonstrating that k_g can be assumed within a 20% range by introducing a negligible error in perfusion estimates and that 10–20 regional time–activity curves appear optimal, the method was validated experimentally by showing its coherence with measured blood tracer levels and with liver perfusion results obtained by an independent technique.

The current approach estimated the hepatic arterial and portal input functions from multiple tissue curves to calculate respective and total organ perfusion. A high

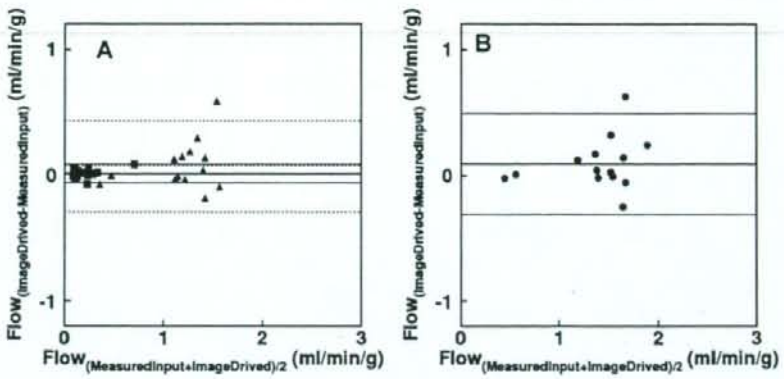

Fig. 9 **a** Bland–Altman plot for arterial (*square*), portal (*triangle*) and **b** total hepatic blood flow differences between measured and image-derived input functions

degree of overlap and tight correlations were observed between the estimated input functions and those obtained during online blood sampling/counting. Consequently, calculated flow values were consistent between the methods. Alternative to the present procedure, a ROI-based input extraction from PET images has been used for the carotid artery in [^{11}C]flumazenil brain studies [27], abdominal artery for kidney blood flow quantification with $H_2{}^{15}O$ [15], and aorta for cardiac ^{18}F-FDG metabolism [32], and for tumor blood using $H_2{}^{15}O$ [34]. In these approaches, ROIs are drawn in visible vessels, and the partial volume effect must be taken into account by testing different ROI sizes or by thresholding the pixels inside arterial ROIs; the need for partial volume correction remains a necessary limitation. Closer to the current analysis, Edward et al. applied multiple tissue curves to estimate quantitative kinetic parameters in the brain [7] and well reproduced the input function for $H_{15}{}^2O$. However, their formula did not take into account the radioactivity from the blood component inside the tissue ROI, and the validity of their method may not be directly extrapolated to the liver because of the large proportion of blood, which is typically ranging between 0.27 and 0.40 ml/ml [23] in this organ. The present method showed that the height of the estimated input is almost doubled if the blood volume is not included in the formula and if the arterial volume contributes 10% of radioactivity in the tissue TACs in our preliminary study (data not shown). The shape of an arterial input function from multiple tissue TACs has been well reproduced in brain ^{18}FDG or [^{11}C]MPDX studies by using an independent component analysis-based method (extraction of the plasma TAC using independent component analysis [24, 25] still requiring one arterial blood sample, and the combination of the latter and the current techniques may be of further simplification and deserves investigation since it would entail neither a model function nor direct blood measurements.

One advantage of introducing a model function was to shape the model input function by imposing constrains to the parameters range, allowing to overcome noise problems caused by limited scan duration and short half-life of ^{15}O. The present approach may be applicable to a study group including subjects with hepatic disorders as far as measurement conditions are equivalent and the shape of the input function can be expected to be similar, though the validity of the present method was tested in normal animals. We

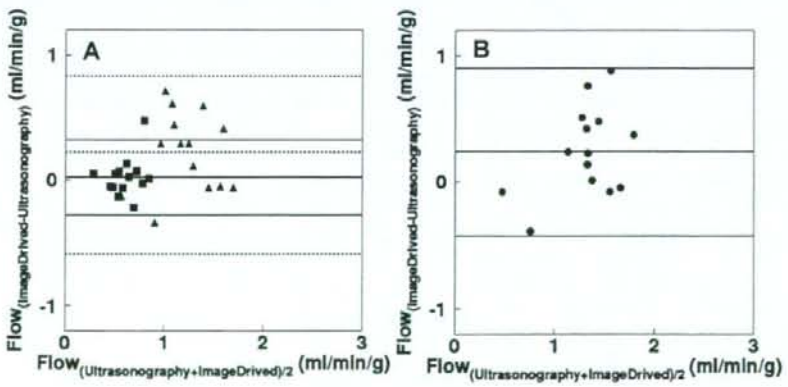

Fig. 10 **a** Bland–Altman plot for arterial (*square*), portal (*triangle*), and **b** total hepatic blood flow differences between ultrasonography and kinetic modeling using image-derived input functions

expect no relevant limitation in the extension of the assumptions concerning the shape to other species and in a majority of hepatic conditions. A drawback in the use of a model function, however, is that the feasibility is unknown for a group in which the shape of input functions could be extremely different or cannot be expressed by the present model function. This is not a commonly expected case. In this situation, the present method would require to, and may still be adapted, by introducing group-specific parameter constraints or a modified model function. The present model function was created by assuming the model, namely, tracer bidirectional diffusion to whole body as in differential Eq. 9. The solution was derived as Eq. 10, and the model function was modified to avoid the one order term of t, which would complicate calculations in the following procedures, i.e., model function for portal input and for tissue response functions. This modification could deteriorate the physiological mean of parameters, such as K_e and K_i; however, the input functions obtained in the present study using this modified equation well reproduced the shape of measured inputs. The modified model function and derived portal model function seemed to be superimposable to measured blood TACs, although there were slight, few-second systematic misalignments in the peak of arterial blood and overestimations at the late phase. This suggested that the error in the position of the peak and in late phase in the estimated input function against measured ones (Figs. 7 and 8) is due to a limitation in the description of the model function.

The present estimation procedure followed two steps, as designed to fit tissue curves individually, and then simultaneously. The first step allowed careful exclusion of tissue TACs showing t_1 or t_2 values over one standard deviation from the mean to eliminate the influence of radioactivity outside the liver region. In fact, in the experimental procedure, $H_2{}^{15}O$ was injected in the femoral vein, draining into the vena cava, which is not distant from the liver. Other adjacent high-perfusion organs include the kidneys. The influence of ROIs drawn in proximity of these regions was not included in the model. Thus, special attention was paid at excluding confounding tissue TACs by examining t_1 and t_2. In the above examples, the tracer was expected to show an early peak in case of an anatomical overlap with the vena cava, and the extracted TAC covering this region was omitted in this step. The second step was introduced to facilitate the achievement of the convergence by fixing the values of t_1, t_2, and r_a to their calculated means (as obtained above) to estimate the remaining two parameters. Generally, if many parameters are estimated in a fitting procedure such as in the present method, there could be many local minima, and uniqueness of parameter solution might not be guaranteed. As shown in the simulation study, the three parameters t_1, t_2, and r_a were estimated independent of the number of tissue TACs; however, the remaining two parameters A and $K_e(1+\alpha)$ were dependent on that. This suggests that correlation among parameters due to their numerosity could not be prevented. However, the shapes of input functions were reproduced, and flow values were consistent with other two methods, i.e., those computed from measured inputs and from ultrasonography. Thus, the correlation among parameters did not seem to affect the estimation of flow values, although further study is required for optimization.

We used a fixed value of k_g to represent the diffusion rate of water between arterial blood and the gut compartment in the estimation of the portal input. The deviation in this rate constant was about 26% in the current study group. The simulation analysis showed that values within 20% of the assumed true k_g number corresponded to a propagated error of 10% in the final estimation of hepatic perfusion. The value of k_g used in our final computations is in accordance with the recently reviewed concept that [20] in mammals, the general biological rate (uptake ratio) varies approximately in proportion to the 3/4 power of body size and, given a body mass of ~60 kg, k_g, which is the uptake rate of water in the gut system, can be predicted to fall around 0.45 min^{-1} in humans. This number is consistent with a mean figure of 0.5 min^{-1}, as obtained in this study, suggesting that the present assumption could be implemented to obtain the liver input function in humans. We also assumed a time delay of portal input to be zero against the arterial one. The deviation in this time was about 0.7 s in the current study group. The simulation analysis showed that an error in this value within 10 s corresponded to a propagated error of less than 10% in the final estimation of hepatic perfusion. Of further strength, a close agreement was shown between estimated and measured blood activity curves and estimated and Doppler-determined liver flow results. The larger difference of the latter result against the former result might be due to the model assumptions in flow calculations, as well as in the assumption of circular shape when estimating the area of the arterial and portal vessels by ultrasonography and in the accuracy of ultrasonography data (from multiple measurements of flow data, coefficient of variation was 13±5% for portal flow and 18± 10% for hepatic arterial flow with this study [data not shown]). In this study, the flow values were calculated assuming the dual input, single compartment model [2, 29, 30, 35]. Altogether, the above observations support the use of a fixed k_g and the current model in the fully non-invasive quantification of liver perfusion.

The validation of the current approach, as obtained in this study, is especially valuable in the liver for multiple reasons. First, the inaccessibility of the portal vein prevents its direct blood sampling in humans. Arterial blood can be obtained [8, 9, 16, 17, 26, 33], but blood counting requires corrections for

dispersion, delay between target organ and sampling device, and cross calibration between PET scanner and radioactivity counter, which are all potential sources of errors, in the same magnitude as that expected with the current method. Second, liver perfusion can be compromised both as consequence and cause of hepatic disease and is considered a prognostic indicator and useful marker during progression or treatment follow-up [6, 22]. Third, the possibility to distinctly quantify portal and arterial perfusion is important because their reciprocal compensation may be masked once only if total hepatic flow is measured.

The present simulation study allowed to establish that the optimal number of tissue TACs for DIF estimation was 10 to 20, independent of the noise levels, among the ones selected in this investigation. As pointed out by Edward et al. [7], as the noise on tissue TACs increased, the standard deviation of uptake ratio of tracer increased. Also, they suggested that the standard deviation tended to decrease when more regions were used. The present study intended to investigate the optimal number of tissue TACs from the whole region of liver. The noise in the liver can be minimized by placing a ROI to cover the whole organ and subsequently dividing it in a number of sub-regions corresponding to 10–20 under the conditions of the current experiments. The present results may depend on the reconstruction method. However, as far as the PET image is calculated quantitatively and the distribution of flow values in the extracted TACs is in the same order of magnitude as the present study, the results of optimization in this study would be applicable because those two conditions were assumed in the present simulation study. We assumed that the ratio of blood flow between the hepatic artery and the portal vein was uniform in the whole organ, as supported by an extended literature on the healthy liver and on a majority of metabolic disorders involving the organ. Conversely, the quantification of flow in hepatic tumors in which perfusion from arterial blood is predominant may be best approximated by simplifying the procedure to a single input or by fitting the relative vascular (arterial and portal) contributions as additional parameters in the model. The current procedure was validated for the determination of liver perfusion with $H_2{}^{15}O$ PET data. Required conditions were a model function to describe the input function and a kinetic model for tracer exchange between blood and tissue. In theory, the present method might be adapted to other tracers and organs if tracer kinetics in the tissue can be described with a model function.

In conclusion, our results demonstrate that arterial and portal vein concentrations of labeled water can be estimated directly from tissue time–activity curves obtained through dynamic $H_2{}^{15}O$ PET imaging. The calculated hepatic arterial, portal, and total perfusion values using estimated or measured input functions were similar and consistent with ultrasonography measurements.

Acknowledgments The authors thank the technical staff of the Turku PET Centre for the efforts and skills dedicated to this project. This work is part of the project Hepatic and Adipose Tissue and Functions in the Metabolic Syndrome (HEPADIP, see http://www.hepadip.org/), which is supported by the European Commission as an Integrated Project under the 6th Framework Programme (contract LSHMCT-2005-018734). The study was further supported by grants from the Academy of Finland (206359 to P.N.), Finnish Diabetes Foundation (P.I.), EFSD/Eli-Lilly (P.I.), Sigrid Juselius Foundation (N.K. and P.I.), and Novo Nordisk Foundation (P.N.).

Appendix

A model function for AIF was created by assuming a two-compartment model in which the tracer is administered in a rectangular form and diffuses bi-directionally between arterial and interstitial space in whole body peripheral tissue compartments. Differential equations for the model function ($C_A(t)$) can be expressed as

$$\frac{dC_A(t)}{dt} = \frac{dF}{dt} - K_e C_A(t) + K_i C_{WB}(t) \tag{9}$$

$$\frac{dC_{WB}(t)}{dt} = K_e C_A(t) - K_i C_{WB}(t) \tag{10}$$

$$\frac{dF}{dt} = \begin{array}{l} A \ (t_1 \le t \le t_2) \\ 0 \ \text{(elsewhere)} \end{array} \tag{11}$$

where t_1 and t_2 assumes the appearance time of administered tracer, and t_2-t_1 represents the administration duration; A corresponds to the given amount of tracer. The equation F (Eq. 11) represents the bolus administration of tracer in the rectangular form with duration t_2-t_1. $C_{WB}(t)$ is the expected tracer concentration in interstitial spaces in whole body peripheral tissues; K_e and K_i are bidirectional tracer diffusion rates between blood and peripheral tissue compartments, respectively. Solving Eq. 10 for C_{WB} gives

$$C_{WB}(t) = K_e e^{-K_i t} \int_0^t C_A(\tau) e^{K_i \tau} \, d\tau. \tag{12}$$

Sum of Eqs. 9 and 10 is

$$\frac{d(C_A(t) + C_{WB}(t))}{dt} = \frac{dF}{dt} \tag{13}$$

Thus,

$$\begin{aligned} C_A(t) + C_{WB}(t) &= F \\ &= 0 \qquad (t < t_1) \\ &= A(t - t_1) \qquad (t_1 \le t \le t_2) \\ &= A(t_2 - t_1) \qquad (t > t_2) \end{aligned} \tag{14}$$

Substitution of C_{WB} from Eq. 12 into 14 after multiplying $e^{K_e t}$ gives

$$e^{K_e t}C_A(t) + K_e\int_0^t C_A(\tau)e^{K_e \tau}d\tau = e^{K_e t}F \quad (15)$$

Differentiation with respect to t after arranging gives

$$\frac{dC_A(t)}{dt} = \alpha F + \frac{1}{K_e}\frac{dF}{dt} - K_e(1+\alpha)C_A(t) \quad (16)$$

where $\alpha = K_f/K_e$. Thus,

$$C_A(t) = K_e e^{-K_e(1+\alpha)t}\int_0^t \left(\alpha F + \frac{1}{K_e}\frac{dF}{dt}\right)e^{K_e(1+\alpha)\tau}d\tau \quad (17)$$

Solving Eq. 17, we obtain

$$\begin{aligned} C_A(t) &= 0 && (t < t_1) \\ &= \frac{A}{K_e^2(1+\alpha)^2}\left(K_e\alpha(1+\alpha)(t-t_1) + 1 - e^{K_e(1+\alpha)(t_1-t)}\right) && (t_1 \le t \le t_2) \\ &= \frac{A}{K_e^2(1+\alpha)^2}\left(K_e\alpha(1+\alpha)(t_2-t_1) + e^{K_e(1+\alpha)(t_2-t)} - e^{K_e(1+\alpha)(t_1-t)}\right) && (t > t_2) \end{aligned} \quad (18)$$

The first term in the second equation for $t_1<t<t_2$, i.e., $K_e\alpha(1+\alpha)(t_1-t_2)$, would complicate further calculations (such as tissue response and portal input); thus, this term was omitted, and the model function (Eq. 18) was modified to set the C_A value as 0 at $t=t_1$, as continuous at $t=t_2$, and as non-zero value at the equilibrium, i.e., at $t=\infty$. Thus, the following equation was derived:

$$\begin{aligned} C_A(t) &= 0. && (t < t_1) \\ &= \frac{A}{K_e^2(1+\alpha)^2}\left(1 - \exp\left(K_e(1+\alpha)(t_1-t)\right)\right) && (t_1 \le t \le t_2) \\ &= \frac{A}{K_e^2(1+\alpha)^2}\left(\exp\left(K_e(1+\alpha)(t_1-t_2)\right) + \exp\left(K_e(1+\alpha)(t_2-t)\right) - 2\cdot\exp\left(K_e(1+\alpha)(t_1-t)\right)\right) && (t > t_2) \end{aligned} \quad (19)$$

References

1. Alenius S, Ruotsalainen U. Bayesian image reconstruction for emission tomography based on median root prior. Eur J Nucl Med. 1997;24:258–65.
2. Becker GA, Muller-Schauenburg W, Spilker ME, Machulla HJ, Piert M. A priori identifiability of a one-compartment model with two input functions for liver blood flow measurements. Phys Med Biol. 2005;50:1393–404.
3. Bland JM, Altman DG. Statistical methods for assessing agreement between two methods of clinical measurement. Lancet. 1986;1:307–10.
4. Blomley MJ, Coulden R, Dawson P, et al. Liver perfusion studied with ultrafast CT. J Comput Assist Tomogr. 1995;19:424–33.
5. Carson RE. Parameter estimation in positron emission tomography. In: Phelps ME, Mazziotta JC, Schelbert HR, editors. Positron emission tomography and autoradiography: principles and applications for the brain and heart. New York, NY: Raven; 1986. p. 347–90.
6. Johnson DJ, Muhlbacher F, Wilmore DW. Measurement of hepatic blood flow. J Surg Res. 1985;39:470–81.
7. Edward VR, Di Bella EV, Clackdoyle R, Gullberg GT. Blind estimation of compartmental model parameters. Phys Med Biol. 1999;44:765–80.
8. Eriksson L, Holte S, Bohm Chr, Kesselberg M, Hovander B. Automated blood sampling system for positron emission tomography. IEEE Trans Nucl Sci. 1988;35:703–7.
9. Eriksson L, Kanno I. Blood sampling devices and measurements. Med Prog Technol. 1991;17:249–57.
10. Henderson JM, Gilmore GT, Mackay GJ, Galloway JR, Dodson TF, Kutner MH. Hemodynamics during liver transplantation: the interactions between cardiac output and portal venous and hepatic arterial flows. Hepatology. 1992;16:715–8.
11. Iida H, Kanno I, Miura S, Murakami M, Takahashi K, Uemura K. Error analysis of a quantitative cerebral blood flow measurement using $H_2{}^{15}O$ autoradiography and positron emission tomography, with respect to the dispersion of the input function. J Cereb Blood Flow Metab. 1986;6:536–45.
12. Iida H, Higano S, Tomura N, Shishido F, Kanno I, Miura S, et al. Evaluation of regional differences of tracer appearance time in cerebral tissues using [^{15}O] water and dynamic positron emission tomography. J Cereb Blood Flow Metab. 1988;8:285–8.
13. Iozzo P, Gastaldelli A, Järvisalo MJ, Kiss J, Borra R, Buzzigoli E, et al. 18F-FDG assessment of glucose disposal and production rates during fasting and insulin stimulation: a validation study. J Nucl Med. 2006;47:1016–22.

14. Iozzo P, Järvisalo MJ, Kiss J, Borra R, Naum GA, Viljanen A, et al. Quantification of liver glucose metabolism by positron emission tomography: validation study in pigs. Gastroenterology. 2007;132:531–42.
15. Juillard L, Janier M, Fouque D, et al. Renal blood flow measurement by positron emission tomography using ^{15}O-labeled water. Kidney Int. 2000;57:2511–8.
16. Kanno I, Iida H, Miura S, Murakami M, Takahashi K, Sasaki H, et al. A system for cerebral blood flow measurement using an $H_2{}^{15}O$ autoradiographic method and positron emission tomography. J Cereb Blood Flow Metab. 1987;7:143–53.
17. Kudomi N, Choi E, Watabe H, Kim KM, Shidahara M, Ogawa M, et al. Development of a GSO detector assembly for a continuous blood sampling system. IEEE TNS. 2003;50:70–3.
18. Kudomi N, Watabe H, Hayashi T, Iida H. Non-invasive estimation of arterial input function for water and oxygen from PET dynamic images. J Nucl Med. 2006;47(Supplement 1):361.
19. Leen E, Goldberg JA, Anderson JR, et al. Hepatic perfusion changes in patients with liver metastases: comparison with those patients with cirrhosis. Gut. 1993;34:554–7.
20. Lindstedt, Schaeffer. Use of allometry in predicting anatomical and physiological parameters of mammals. Laboratory Anim. 2002;36:1–19.
21. Martin-Comin J, Mora J, Figueras J, et al. Calculation of portal contribution to hepatic blood flow with 99m-Tc-microcolloids. A noninvasive method to diagnose liver graft rejection. J Nucl Med. 1988;29:1776–80.
22. Materne R, Van Beers BE, Smith AM, Leconte I, Jamart J, Dehoux JP, et al. Non-invasive quantification of liver perfusion with dynamic computed tomography and a dual-input one-compartmental model. Clin Sci (Lond). 2000;99:517–25.
23. Munk OL, Bass L, Roelsgaard K, Bender D, Hansen SB, Keiding S. Liver kinetics of glucose analogs measured in pigs by PET: importance of dual-input blood sampling. Nucl Med. 2001;42:795–801.
24. Naganawa M, Kimura Y, Nariai T, et al. Omission of serial arterial blood sampling in neuroreceptor imaging with independent component analysis. NeuroImage. 2005a;26:885–90.
25. Naganawa M, Kimura Y, Ishii K, Oda K, Ishiwata K, Matani A. Extraction of a plasma time–activity curve from dynamic brain pet images based on independent component analysis. IEEE Trans on Bio-Med Eng. 2005b;52:201–10.
26. Ruotsalainen U, Raitakari M, Nuutila P, Oikonen V, Sipilä H, Teräs M, et al. Quantitative blood flow measurement of skeletal muscle using oxygen-15-water and PET. J Nucl Med. 1997;38:314–9.
27. Sanabria-Bohorquez SM, Maes A, Dupont P, Bormans G, de Groot T, Coimbra A, et al. Image-derived input function for [^{11}C] flumazenil kinetic analysis in human brain. Mol Img Biol. 2003;5:72–8.
28. Taniguchi H, Oguro A, Takeuchi K, Miyata K, Takahashi T, Inaba T, et al. Difference in regional hepatic blood flow in liver segments—non-invasive measurement of regional hepatic arterial and portal blood flow in hufnan by positron emission tomography with H2(15)O. Ann Nucl Med. 1993;7:141–5.
29. Taniguchi H, Oguro A, Koyama H, Masuyama M, Takahashi T. Analysis of models for quantification of arterial and portal blood flow in the human liver using PET. J Comput Assist Tomogr. 1996a;20:135–44.
30. Taniguchi H, Koyama H, Masuyama M, Takada A, Mugitani T, Tanaka H, et al. Angiotensin-II-induced hypertension chemotherapy: evaluation of hepatic blood flow with oxygen-15 PET. J Nucl Med. 1996b;37:1522–3.
31. Taniguchi H, Yamaguchi A, Kunishima S, Koh T, Masuyama M, Koyama H, et al. Using the spleen for time-delay correction of the input function in measuring hepatic blood flow with oxygen-15 water by dynamic PET. Ann Nucl Med. 1999;13:215–21.
32. Van der Weerdt A, Klein LJ, Boellaard R, Visser CA, Visser FC, Lammertsma AA. Image-derived input functions for determination of MRGlu in cardiac ^{18}F-FDG PET scans. J Nucl Med. 2001;42:1622–9.
33. Votaw JR, Shulman SD. Performance evaluation of the pico-count flow-through detector for use in cerebral blood flow PET studies. J Nucl Med. 1998;39:509–15.
34. Watabe H, Channing MA, Riddell C, Jousse F, Libutti SK, Carrasquillo JA, et al. Noninvasive estimation of the aorta input function for measurement of tumor blood flow with. IEEE Trans Med Imaging. 2001;20:164–74.
35. Ziegler SI, Haberkorn U, Byrne H, Tong C, Kaja S, Richolt JA, et al. Price P Measurement of liver blood flow using oxygen-15 labelled water and dynamic positron emission tomography: limitations of model description. Eur J Nucl Med. 1996;23:169–77.